



In-situ hot forging directed energy deposition-arc of CuAl8 alloy[☆]

Valdemar R. Duarte^{a,*}, Tiago A. Rodrigues^a, N. Schell^b, R.M. Miranda^a, J.P. Oliveira^{a,c}, Telmo G. Santos^a

^a UNIDEMI, Department of Mechanical and Industrial Engineering, NOVA School of Science and Technology, Universidade NOVA de Lisboa, 2829-516 Caparica, Portugal

^b Institute of Materials Physics, Helmholtz-Zentrum Hereon, Max-Planck-Str. 1, D-21502 Geesthacht, Germany

^c CENIMAT/13N, Department of Materials Science, NOVA School of Science and Technology, Universidade NOVA de Lisboa, 2829-516 Caparica, Portugal

ARTICLE INFO

Keywords:

CuAl8 alloy
Directed energy deposition-arc
Forging
Viscoplastic deformation
Grain refining

ABSTRACT

CuAl8 alloy finds applications in industrial components, where a good anti-corrosion and anti-wearing properties are required. The alloy has a medium strength and a good toughness with an elongation to fracture at room temperature of about 40%. Additionally, it has a good electrical conductivity, though lower than that of pure Al or pure Cu. Despite these characteristics, additive manufacturing of the CuAl8 alloy was not yet reported. In this work, the direct energy deposition-arc (DED-arc) with and without *in-situ* hot forging was used to determine the microstructure evolution and mechanical properties. No internal defects were seen on the parts produced. Hot forging combined with DED-arc was seen to reduce and homogenize the grain size, improve mechanical strength and isotropy of mechanical properties. Moreover, the use of this novel DED-arc variant was seen to reduce the magnitude of residual stresses throughout the fabricated part. We highlight that this alloy can be processed by DED-arc, and the hot forging operation concomitant with the material deposition has beneficial effects on the microstructure refinement and homogenization.

1. Introduction

Additive Manufacturing (AM) is being intensively investigated by several research groups due to the intrinsic characteristics technological processes that are in line with industrial digitalization, reduction of energy and raw materials consumption and clean forms to manufacture goods [1,2]. Directed Energy Deposition process category as defined by international standards, is also commonly known as wire and arc additive manufacturing (WAAM). From the wide range of AM processes for metallic alloys, WAAM is eventually the least expensive as it uses an electric arc as the heat source. Moreover, the equipment and the well-consolidated knowledge from arc welding technology and welding metallurgy are readily applied in WAAM [3].

In multiple pass arc welding of metallic materials without solid state transformations, the development of coarse-grained structures by epitaxy is well known. The same is observed in multilayer WAAM

process. Solidification structures, either cellular dendritic or columnar ones, develop through the successive layers and this is typically accompanied by a detrimental effect on the mechanical properties and performance of the fabricated components [4].

Several groups have developed variants based on plastic deformation and active cooling to improve the as-deposited microstructure [5–8]. Regarding the plastic deformation variants they can be categorized accordingly to the temperature at which they are performed (hot or cold) and considering how they are applied, *i.e.* continuously or discontinuously.

The developments in continuously hot deformation during WAAM usually comprises a roller that follows the torch at a fixed distance and deforms the material at high temperatures. Zhang et al. [9] studied the effects of the roller-heat source distance on the samples surface aspect and verified that for a short distance, the deformation temperature is too high and the material adhere to the roller and instead of being deformed

Abbreviations: AM, Additive Manufacturing; DED-arc, Direct Energy Deposition-arc; FCC, Face-Centred Cubic; BCC, Body-centered cubic; GMAW, Gas Metal Arc Welding; HF-WAAM, Hot Forging WAAM; NDT, Non-Destructive Testing; WAAM, Wire and Arc Additive Manufacturing.

[☆] One of the authors of this article is part of the Editorial Board of the journal. To avoid potential conflicts of interest, the responsibility for the editorial and peer-review process of this article lies with the journal's other editors. Furthermore, the authors of this article were removed from the peer review process and had no, and will not have any access to confidential information related to the editorial process of this article.

* Corresponding author.

E-mail address: v.duarte@campus.fct.unl.pt (V.R. Duarte).

<https://doi.org/10.1016/j.addma.2022.102847>

Received 21 January 2022; Received in revised form 18 April 2022; Accepted 20 April 2022

Available online 25 April 2022

2214-8604/© 2022 The Authors. Published by Elsevier B.V. This is an open access article under the CC BY-NC license (<http://creativecommons.org/licenses/by-nc/4.0/>).

it is dragged by the roller, resulting in a bad final surface aspect. In contrast, at a higher distance the deformation is insufficient due to the high cooling rate and the lower rolling force. Therefore, a fine tuning of the roller-heat source distance must be performed. Despite the difficulties in tuning the deformation parameters several authors have reported that continuously hot deformation variant is able to refine the microstructure, Nickel-based superalloy 718 [10] and the Ti-6Al-4 V alloy [11].

However, the continuously hot deformation using a roller have limited applications, since the rolling system cannot rapidly change the direction, it limits its positioning, increases the complexity of the deposition path, or even makes it impossible to produce some complex geometries.

With regard to the *in-situ* discontinuous hot forming variants, most authors used systems similar to the hammer peening technique, where an electromagnetic actuator [12], or a pneumatic cylinder [13], are coupled to a steel impact tool used to deform the bead surface. Ye et al. [14] applied a discontinuous hot forming during the production of Ti-6Al-4 V alloy, and verified that it causes a microstructural recrystallization forming an equiaxed structure with reduced the grain size, and improves the microhardness of top surface. However, it was verified that the developed system was promoting the formation of defects such as pores and cracks, and have only studied the effects of the deformation on single bead, the effect of the following deposition on the recrystallized microstructure was not studied. With the same mechanism Li et al. [15] studied the effects on microstructure of single-bead GH3039 superalloy, achieving also a grain refinement and an increase of 46% in the material microhardness, attributed to the dynamic recrystallization induced by the plastic deformation.

Duarte et al. [13] developed a variant based on *in-situ* hot forging in the viscoplastic regime with considerably lower loads than the used in the variants presented above, and described the fundamentals of the process. It encompasses a linear hammer, with a stroke of about 10 mm and operating at 5–10 Hz, that performs a locally viscoplastic deformation of the already deposited layers immediately after the material is deposited. By plastically deforming the as-deposited layer at high temperature, dynamic recrystallization of the previous layer is promoted. Moreover, process-related defects such as pores, can be eliminated, and the resulting flat surface facilitates the application of Non-Destructive

Testing (NDT) [16]. Therefore, by applying deformation while the material is at high temperatures (in its viscoplastic regime) the aforementioned features can be achieved with a fraction of the load that would be required if the deformation was performed at low temperatures, *i.e.*, near room temperature.

The presence of recrystallized grains in WAAM manufactured parts has several advantages: first, it can increase the mechanical strength following the Hall–Petch relationship; then, the existence of refined grains at the top of the deposited layer provides a higher density of nucleation sites, thereby decreasing the susceptibility to large grain growth as typically observed in WAAM deposits. This is particularly relevant for alloys without solid state transformations, which are more susceptible to significant grain growth during successive thermal cycles [3].

Linear *in-situ* discontinuous hot forming variants were already designed and tested with very promising results, but the linearity of the systems has two major shortcomings: it imposes a limitation of the part geometries to linear ones, and the contact area between the hammer and the material surface forged was restricted. Thus, in this work, a new hammer was designed as a circular crown placed concentrically with the welding nozzle (refer to Fig. 1) allowing to forge nonlinear deposition paths since the forging action is independent of the travel direction of the torch. The developed equipment characterized and the impact of *in-situ* Hot Forging WAAM (HF-WAAM) on the microstructure and mechanical properties was probed by microscopy, high energy synchrotron X-ray diffraction, electric conductivity, and mechanical testing.

2. *In-situ* Hot Forging WAAM torch description

The technological aspects of the innovative WAAM variant (patented by the authors of this research [17]) comprises a pneumatic system that actuates the hammer tip and forges the material immediately after its deposition. The hammer (detailed in Fig. 1) is actuated by two pneumatic actuators placed symmetrically to avoid discrepancies in the generated forces. The pneumatic system consists of: two Festo ADN-12-10-I-P-A pneumatic cylinders; one Festo MS-LFR air filter; one pressure regulator and gauge; and one 5/2-way bi-stable solenoid valve Festo VUVS-LK20. Hot forging during deposition requires the control of a set of process parameters that may influence the material condition,

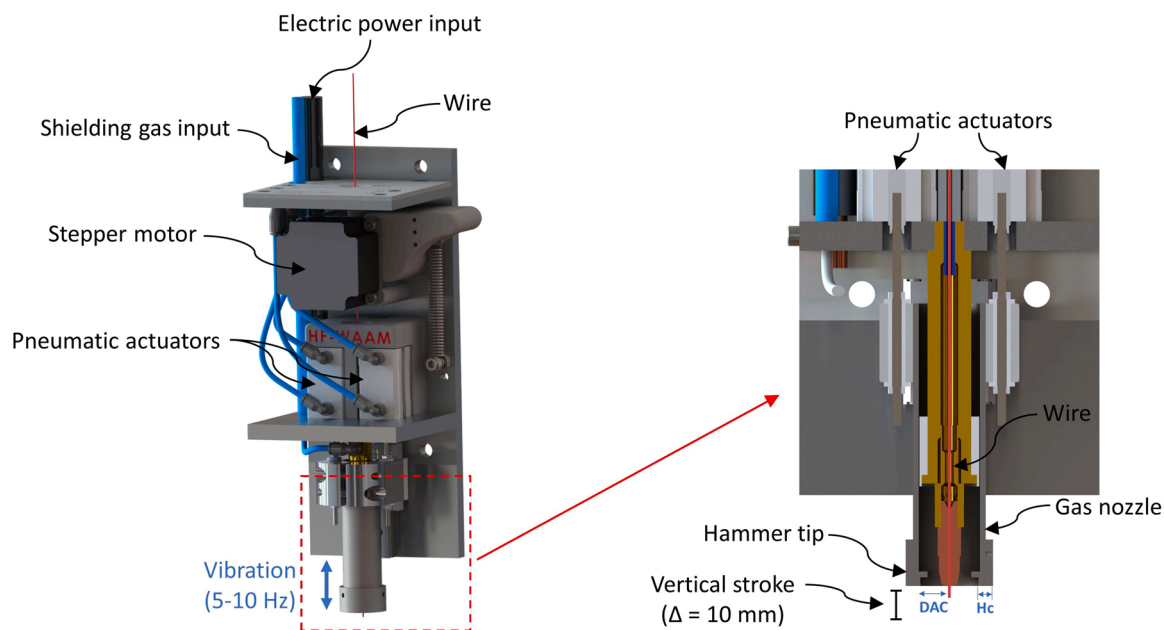


Fig. 1. Schematic representation of the developed torch for *in-situ* Hot Forging WAAM (HF-WAAM). A video of the system can be seen in supplementary material section (temporarily here: Folder).

geometry, as well as metallurgic and mechanical properties. These include forging force, F_f [N]; forging frequency, F_f [Hz]; distance to arc centre (DAC) [mm], and hammer geometry. Concerning the DAC, it is necessarily defined by the radius of the hammer tip (Fig. 2b).

The area forged in each hammer stroke depends on the bottom surface geometry of the hammer and the forging step, F_s [mm], (*i.e.*, the distance, in millimeters, travelled by the hammer in one cycle); which is a function of the F_f and the travel speed, TS [mm/s]. Thus, the forging step is given by Eq. (1).

$$F_s = \frac{1}{F_f} \times TS \quad (1)$$

Since the hammer has a circular crown shape, the forging step must be lower than the crown thickness to avoid unforged areas between consecutive steps. To determine the applied forging pressure, it is necessary to identify the forged area during each cycle. For this particular geometry, the forged area is represented in Fig. 2 and can be easily estimated by Eq. (2), where F_s [mm] is the above-mentioned forging step (Eq. 1) and L_w [mm] is the arc length defined by the contact between the hammer circular crown and the deposited material. The L_w [mm] can be computed by Eq. (3), where R_m [mm] is the hammer internal radius and β [°] is the angle of the arc half-length. β [°] can be computed by Eq. (4), where W [mm] is the bead width.

$$A = F_s \times L_w \quad (2)$$

$$L_w = \frac{2\pi R_m \times 2\beta}{360} \quad (3)$$

$$\beta = \sin^{-1}\left(\frac{W}{2R_m}\right) \quad (4)$$

Another important feature of the hammer is the dimension of the circular hammer crown, H_c [mm], compared to the forging step, F_s [mm]. In fact, H_c must be greater than F_s to assure that the previously deformed material will act as a mechanical stopper, avoiding excessive deformation of the viscoelastic deposited material (Fig. 2). This promotes a continuous flat surface, that is highly dependent on the material temperature. Slight deviations of this temperature promote different forging depths, and therefore, an uneven upper surface. Three videos of the *In-situ* Hot Forging WAAM torch can be seen in supplementary material section (temporarily here: Folder).

3. Dynamic characterization of the forging system

The speed of the hammer when it touches the deposited material, is an important variable of the forging process, as it determines the kinetic energy carried by the hammer, that is later absorbed by the as-deposited layer under the form of deformation. The speed of the hammer also

determines the forging force. The theoretical final speed of the hammer, v_f [m/s], can be calculated using the equations of the uniformly accelerated motion (Eq. 5), where: a [m/s^2] is the hammer acceleration and ΔY [m] is the vertical distance traveled by the hammer, correspondent to the stroke of the pneumatic cylinders.

$$v_f = \sqrt{2a\Delta Y} \quad (5)$$

However, the hammer's acceleration is difficult to compute due to the unknown friction in the moving parts and the unknown real dynamic pressure inside the pneumatic cylinders. Therefore, an alternative approach to measure the final speed of the hammer is needed. The velocity was experimentally measured, and the dynamic characterization of the forging mechanism was performed by high-speed imaging. The acquisition of the images was obtained during the vertical movement of the forging system, when a sample was being produced. This method was chosen over others, as it allows the simultaneous evaluation of several factors, such as: the material strain rate, the estimation of the impact force, and the evaluation of the overall performance of the forging system.

A video of the movement of the hammer was acquired using a high-speed camera (Photron Mini WX50) operating at 10,000 fps and 512×256 pixels, thus having a temporal resolution of 0.1 ms and a spatial resolution of 0.0382 mm Fig. 3a) depicts the schematic representation of the movement of the hammer during forging. It operates according to 4 distinct stages (also refer to Fig. 3b)): 1-hammer is stopped at the top position; 2-hammer is descending with increasing velocity; 3-hammer is forging; and 4-hammer is moving up. It is worth to notice that a duty cycle of 20% is used to reduce the time contact between the hammer and the hot deposited material.

From the acquired data (Fig. 3c)), it was observed that the impact contact between the hammer and the part occurs almost instantaneously during a very short period (δt). The material deformation starts when the hammer comes into contact with the as-deposited layer. Although the hammer has acceleration through its descent movement, the instantaneous velocity before impact can be computed by $V = \Delta y/\Delta t$, since at this stage of the movement the velocity of the hammer is almost constant (Fig. 3c)). During this initial deformation, the deposited material loses its natural convex shape and accommodates to the planar surface of the hammer, increasing the contact area and therefore the resistance the material imposes to the hammer movement (Fig. 3a)). With the increase of this resistance during δt , the hammer starts to decelerate until it comes into contact with the previously deformed material which is at a lower temperature and acts as a stop for the hammer (stage 3).

The last stage of the deformation is critical in the process, since it is at this stage of deformation, when the hammer decelerates, and the hammer kinetic energy is transferred to the part in production. It must

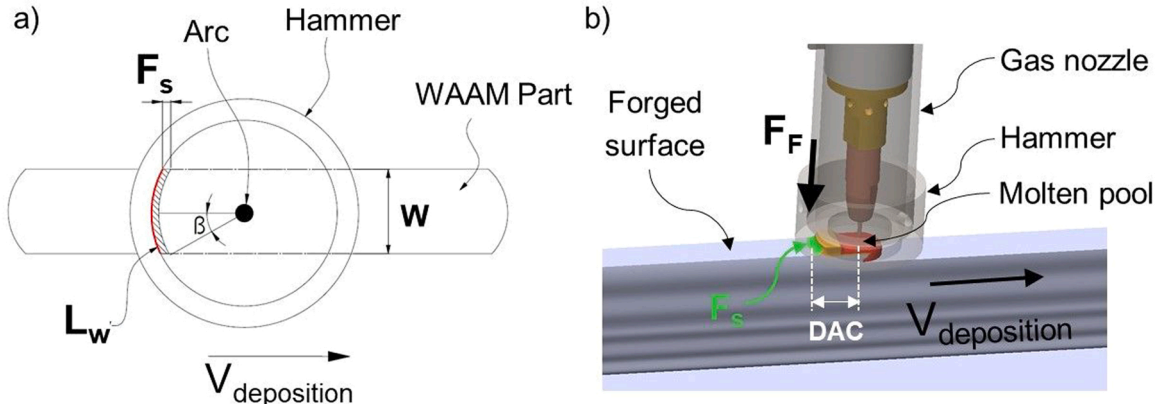


Fig. 2. Schematic representation of the forged area at each step: a) top view (2D), b) isometric view (3D). The forged projected area is computed by Eq. (2).

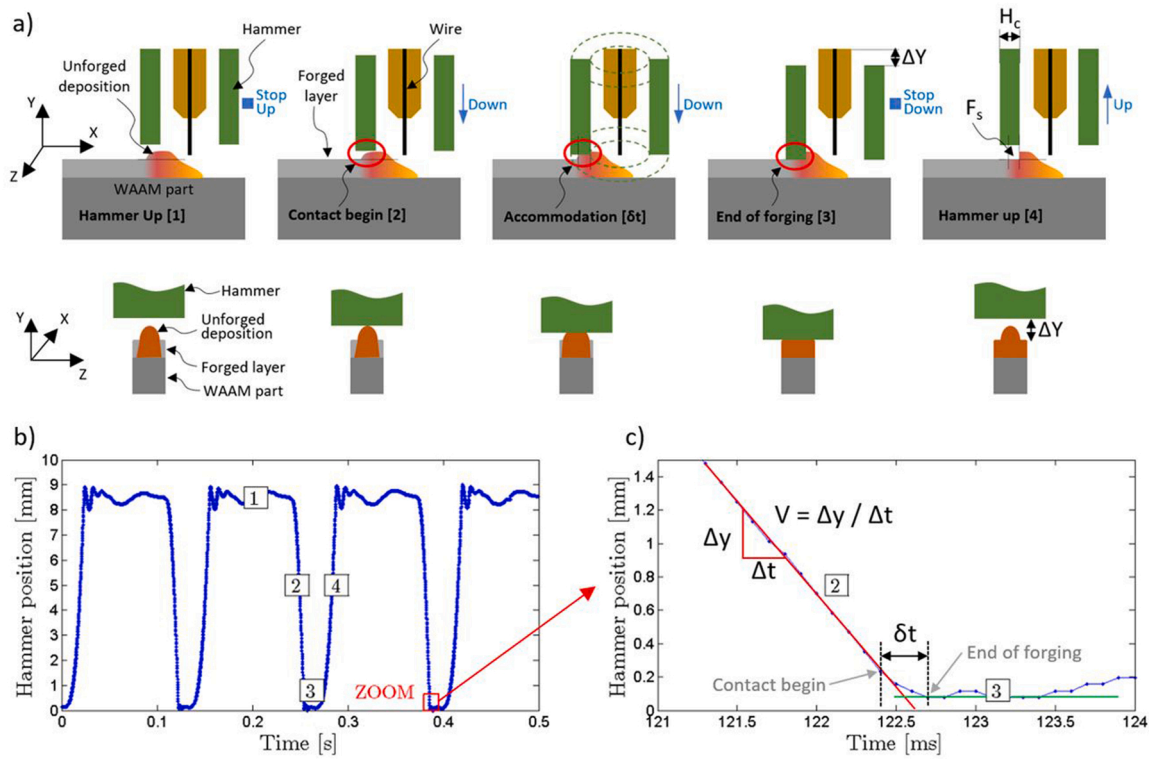


Fig. 3. Dynamics of the *in-situ* HF-WAAM during a deposition with forging at $F_f = 8$ Hz and a duty cycle of 20%. a) Schematic representation of the movement of the hammer during forging, b) Hammer position along the time during the deposition and forging of a sample acquired at 10,000 fps, c) Zoom of b). A video of the forging deposition can be seen in supplementary material section (temporarily here: Folder).

be noticed that the forging force is not a static force, resulting from the static pressure provided by the pneumatic actuators; it is rather an impact force, resulting from the almost instantaneous impact of the mass of the hammer into the deposited material. Consequently, the forging force is considerably higher than the actuating force (pressure \times area) of the pneumatic actuators.

Thus, the impact forging force depends on: the hammer speed before contact ($V = \Delta y / \Delta t$) and the impact time, δt , both represented in Fig. 3c). It can be estimated by using the principle of impulse and momentum (Eq. 6), where I [N·s] is the impulse, P [N·s] is the linear momentum, m [kg] is the mass of the moving hammer parts, Δv [m/s] is the difference between the initial and final velocity of the forging hammer,

F_{avg} [N] is the average force during the impact (forging), and δt [s] is the time duration of the impact.

$$I = \Delta P = m \cdot \Delta v = F_{avg} \cdot \delta t \quad (6)$$

In the present case, the mass of the moving parts of the torch is 0.435 kg, the average experimental impact time, δt is 0.475 ms, and the final velocity of the hammer is 1.12 m/s. Therefore, the average impact force is of 1026 N. The forging strain rate is 322.2 s^{-1} , considering a plane strain compression in the plane ZOY with the initial and the final layer height of 1.45 and 1.27 mm, respectively.

Considering an average measured width of the hot forged sample of 7.3 ± 0.3 mm and that the forging step is of 0.75 mm (*i.e.* in each stroke

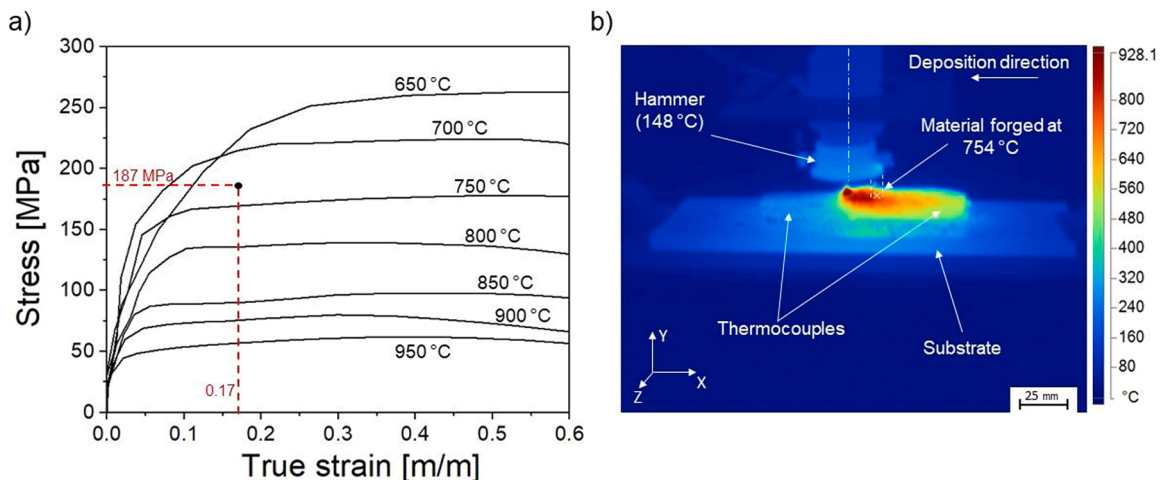


Fig. 4. Stress-strain curves at various temperatures for the CuAl alloy (a); thermogram of the deposition, with the identification of the hammer temperature and the material temperature while forged (b).

the hammer advances 0.75 mm), the area that is forged in each hammer stroke is 5.475 mm². Thus, the stress exerted by the hammer in the deposited material is of about 190 MPa.

Fig. 4 details typical flow-stress curves for this alloy obtained at a strain rate of 5 s⁻¹, as well as the values of the stress and strain achieved during the *in-situ* hot forging. Despite the difficulty in obtaining the flow stress curves of this material at strain rates near those experienced by the material, the following qualitative conclusions are valid, as the increase of the strain rate increases the material flow value stress.

An equivalent true strain of 0.17 was achieved during the *in-situ* hot forging which was calculated using the measurements of the layer height of the hot-forged and as-built samples. By superimposing the calculated true strain and the stress exerted by the hammer (190 MPa) on the flow stress curves of this material (refer to Fig. 4a)), it is possible to verify that the hot forging must occur while the material is in the 700–750 °C temperature range. Additionally, the thermographic analysis shown in Fig. 4b) confirms that the material is forged at a temperature of 750 °C. It is also observed that the hammer does not exceed a temperature of 150 °C, which justifies the choice of a tool steel for the hammer material, since at this temperature the material does not lose its properties.

Since the melting temperature range of this alloy is between 1053 and 1100 °C, it can be concluded that it is possible to increase the deformation imposed on the material by reducing the diameter of the hammer, which implies that the material is forged while it is at a higher temperature, since the stress applied will remain constant, or through the increase of the forging frequency, which makes that in each hammer strike the forged area is smaller and therefore the applied stress increases.

Thus, it is demonstrated that the developed *in-situ* hot forging system can be adjusted as needed, and plastic deformation during WAAM can be performed with the material at different temperatures which in turn allows to tune the amount of deformation imposed during the processing and control the microstructure evolution, *i.e.*, by preferentially inducing strain hardening, if forging is applied at low temperature, or by promoting dynamic recrystallization when the deformation is at high temperature regimes.

4. Materials and methods

The material used in this research was a CuAl8 alloy which is a copper-based alloy with 8.5 wt% of aluminium. It also contains a small addition of iron that promotes the formation of precipitates homogeneously distributed throughout the structure acting as grain refiners during solidification, thus improving the alloy mechanical properties [18]. The chemical composition of the alloy is depicted in Table 1.

The setup used to produce the samples consisted of a customized DED-Arc torch attached to a moving head within a working envelope of 2760 × 1960 × 2000 mm³. A PRO MIG 3200 power source from KEMPY was used to deposit 1 mm diameter wire of CuAl8 on a mild steel substrate.

For the dynamic characterization, a Photron FASTCAM Mini WX50 high-speed camera equipped with a Nikon AF IKKOR 28–105 mm macro lens was used. To ensure the required levels of lighting, four 100 W LED floodlights from V-TAC were used. The data obtained with the high-speed camera was processed using a Python-based software, in which each acquired frame is binarized with a threshold function, and the position of the forging system is targeted.

Two sets of samples, one as-built and the other hot forged were produced to study the effect of hot forging. The length of each produced sample was fixed at 100 mm and the time interval between layers was

Table 1
Chemical composition of the CuAl8 wire [wt%].

| | Cu | Al | Mn | Ni | Fe |
|-------|------|-----|-------|-------|----|
| CuAl8 | Bal. | 8.5 | < 1.0 | < 1.0 | 1 |

fixed at 15 s. The walls were built with a zig-zag deposition strategy, wherein the deposition of a layer started at the end point of the previous one.

The process parameters were the same for both samples and are detailed in Table 2, the only difference being the application of the hammer forging in one of the samples.

Cross-sections from the center of each sample were cut, polished and etched. A Leica DMI 5000 M inverted optical microscope was used to analyze the microstructural features. The estimation of phase percentage was done using a Python software developed in-house. Hardness tests were performed with a load of 4.9 N along the part height. The distance between indentations was of 1 mm.

Electrical conductivity was assessed by eddy current measurements to evaluate the effect of the *in-situ* hot forging on this property, relevant for electromagnetic applications, and provide a complementary information to hardness [19]. An Olympus Nortec 600D impedance measurement equipment and an absolute helical shielded EC probe, with 3 mm diameter, operating in bridge mode, were used. The test frequency was set at 350 kHz, and the angle at 219° to align the imaginary axis with the variations in electrical conductivity.

Uniaxial compressive tests were performed on an Autograph Shimadzu machine model AG500Kng equipped with a Shimadzu load cell SFL-50 kN AG with a total capacity of 50 kN. A crosshead displacement speed of 0.01 mm/s was imposed. Three specimens for each condition were evaluated. Reduced specimens for mechanical testing had to be used due to the dimensions of the built part. These were removed from vertical and horizontal directions of both samples.

Thermal analysis was performed with a thermographic infrared (7.5 – 14 μm wavelength) camera Fluke TI400 to monitor the temperature of the sample and hammer. The camera had an accuracy of ± 2 °C, a measurement limit of – 20–1200 °C, a refresh rate of 9 Hz, and a resolution of 320 × 240 pixel. The emissivity was set to 0.62, previously validated using thermocouples.

X-ray diffraction was performed at beamline P07 of the High Energy Materials Science (HEMS), PETRA III/DESY, using a wavelength of 0.1423 Å (87.1 keV) and an incident beam of 1 × 1 mm. A Perkin-Elmer detector, with a pixel size of 200 × 200 μm², was placed at 1.40 m from the sample. LaB6 powder was used for calibration. The raw 2D Debye-Scherrer images provide qualitative information on the grain size and texture of the analyzed material [15].

Moreover, from the X-ray diffraction tests performed, the residual stresses of both as built and hot forged samples were calculated. An in-house python-based routine with the xrdfit package [20] was used to implement a Pseudo-Voigt profile function to fit the diffraction peaks and extract, for each analyzed point, the position of the peak situated at 2θ = 4.4° which corresponds to the face-centered cubic Cu phase (FCC-α), the predominant phase present on both samples, as observed in the diffractogram presented in Fig. 9.

In each sample, the scans were performed in the centerline of the wall cross section. The scans started in the interface between the substrate and the deposited material and finished at the top of the wall, with

Table 2
Process parameters used during the deposition.

| Deposition parameters | |
|------------------------------|------------------------|
| Welding mode | GMAW – continuous mode |
| Number of layers | 10 |
| Wire feed speed | 4 m/min |
| Travel speed | 360 mm/min |
| Voltage | 19 V DC + |
| Contact tip to work distance | 9 mm |
| Shielding gas | Argon 99.99% |
| Gas flow rate | 15 l/min |
| Hot forging parameters | |
| Forging frequency | 8 Hz |
| Forging pressure | 0.5 MPa |
| Distance to arc center | 12.5 mm |

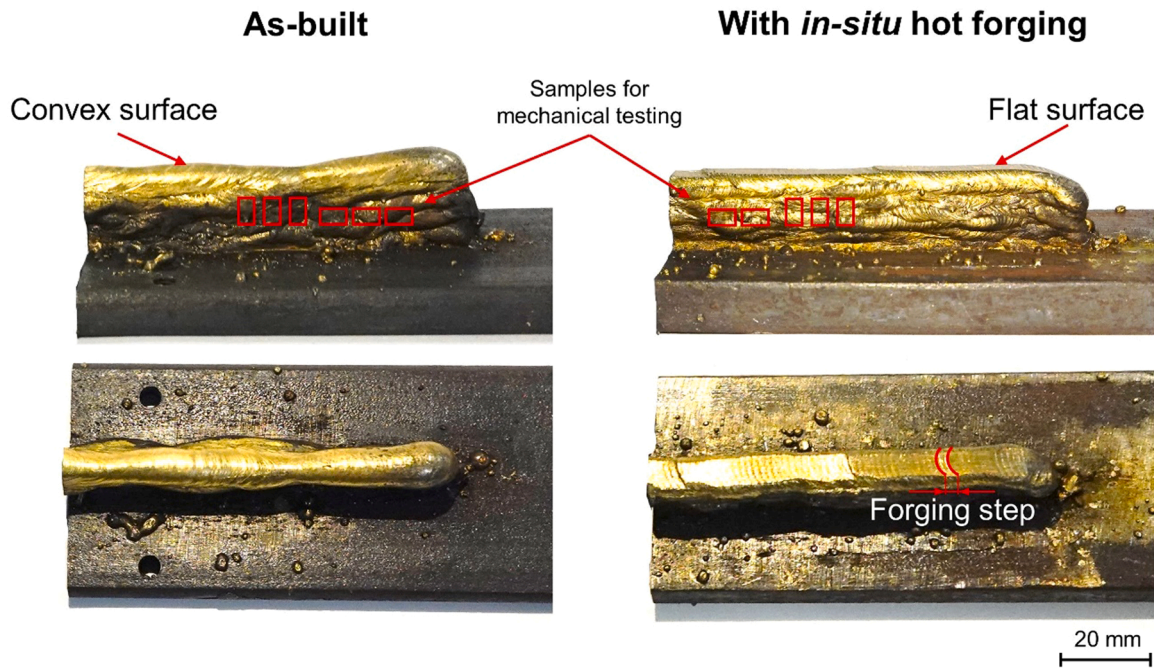


Fig. 5. Photograph of the as-built and *in-situ* hot forged samples showing the upper and side surfaces of the as-built walls.

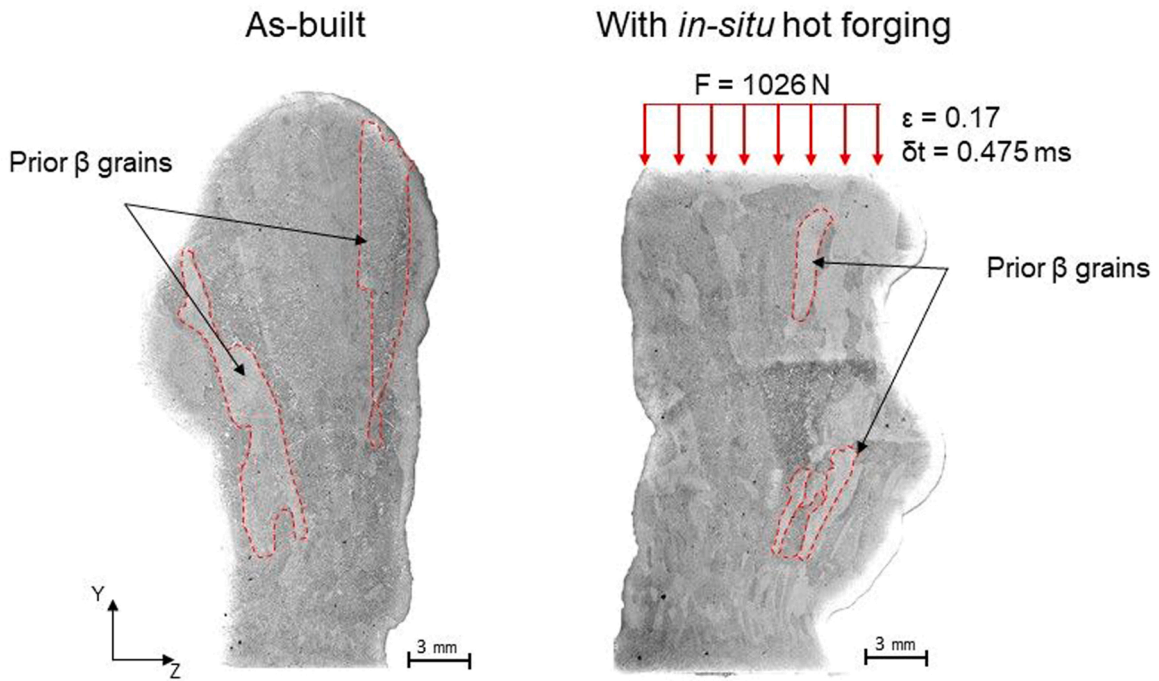


Fig. 6. Macrographs of parts built without and with hot forging showing the geometrical features.

each point spaced by 0.5 mm from the previous one.

The specific direction lattice spacing (d_k) was calculated from the peak position of each acquired point (k), according to the Bragg's law (Eq. 7).

$$d_k = \frac{\lambda}{2\sin\theta_k} \quad (7)$$

where θ_k is the peak maximum position and λ is the beam wavelength (0.1423 Å).

The accurate determination of the stress-free lattice spacing (d_0) is of

great importance to calculate the absolute value of the measured residual stresses, however, for this material it has not yet been reported in the bibliography. Moreover, it is expected that the stress-free lattice spacings vary as a function of position [21], and to accurately measure it, it would be necessary to cut a series of small stress-free cubes to determine d_0 in each analysed point. Therefore, since the goal of this work is to evaluate the relative changes that hot forging may promote on the deposited material in comparison to the conventional WAAM process, the stress-free lattice spacing considered for the following calculations was the average of the lattice space measured along the centre line of the as-built sample integrated along the full azimuthal angle.

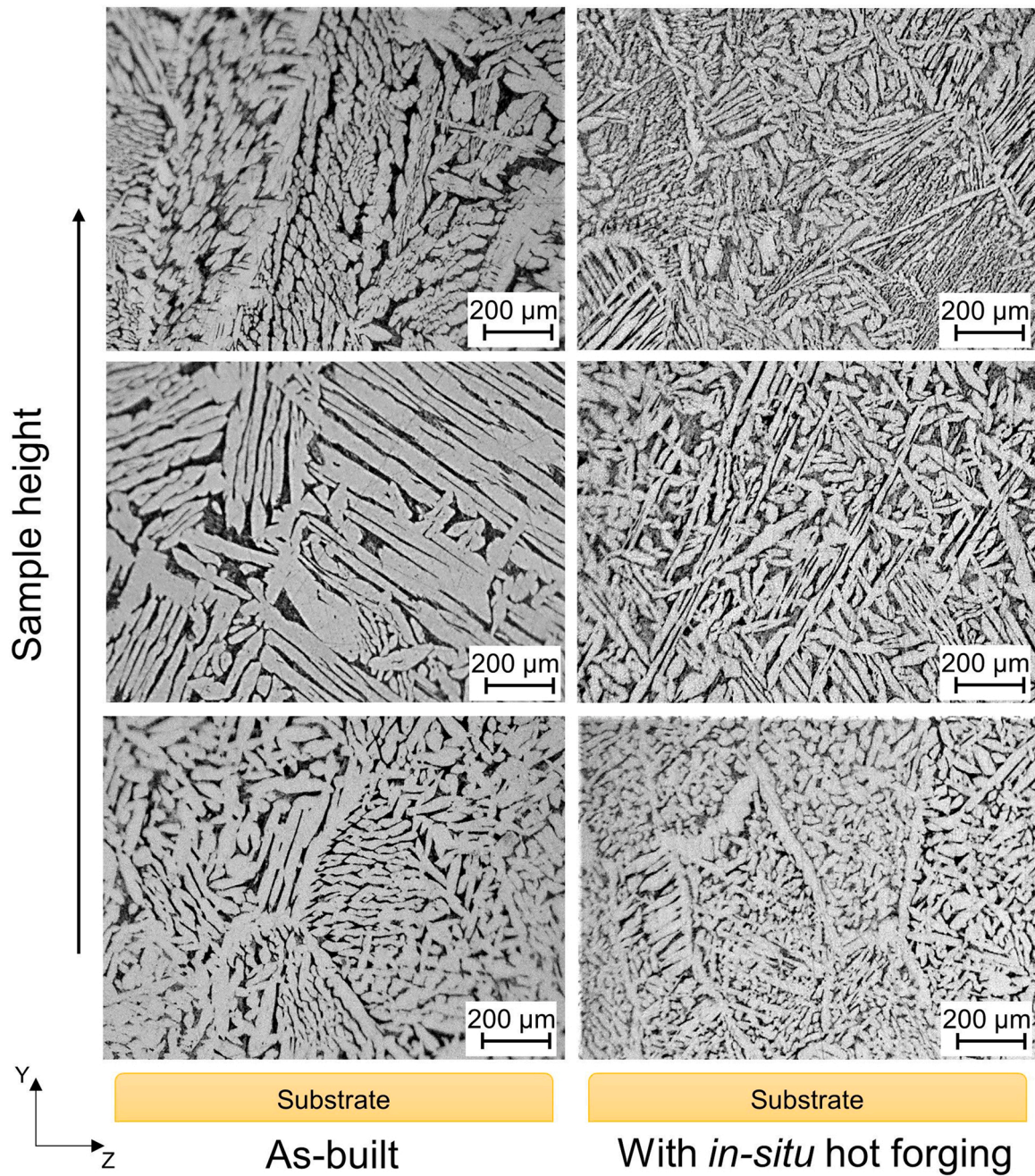


Fig. 7. Microstructure of samples produced: as built and with hot forging. α phase (white) and β (dark).

From the azimuthal integration at 0 and 90° for each analyzed point, it is only possible to obtain the values of d_k^x and d_k^y , respectively. Therefore, the value of the lattice spacing in the d_k^z direction (sample thickness) can be calculated by Eq. (8).

$$d_0 = \frac{1-\nu}{1+\nu}d_k^z + \frac{\nu}{1+\nu}(d_k^x + d_k^y) \quad (8)$$

where the poisson coefficient $\nu = 0.328$ [22].

Then, the principal strains (ϵ) can be computed from the distance between adjacent oriented planes of atoms [23], using the crystal lattice as:

$$\epsilon_{xx,k} = \frac{d_k^x - d_{0,k}}{d_{0,k}} \quad (9)$$

$$\epsilon_{yy,k} = \frac{d_k^y - d_{0,k}}{d_{0,k}} \quad (10)$$

$$\epsilon_{zz,k} = \frac{d_k^z - d_{0,k}}{d_{0,k}} \quad (11)$$

Once the three principal strain components are computed the principal stresses (σ) on each plane can be calculated using the triaxial form of the Hooke's Law (Eqs. 12–14).

$$\sigma_{xx,k} = \frac{E}{(1+\nu)(1-2\nu)} [(1-\nu)\epsilon_{xx,k} + \nu(\epsilon_{yy,k} + \epsilon_{zz,k})] \quad (12)$$

$$\sigma_{yy,k} = \frac{E}{(1+\nu)(1-2\nu)} [(1-\nu)\epsilon_{yy,k} + \nu(\epsilon_{xx,k} + \epsilon_{zz,k})] \quad (13)$$

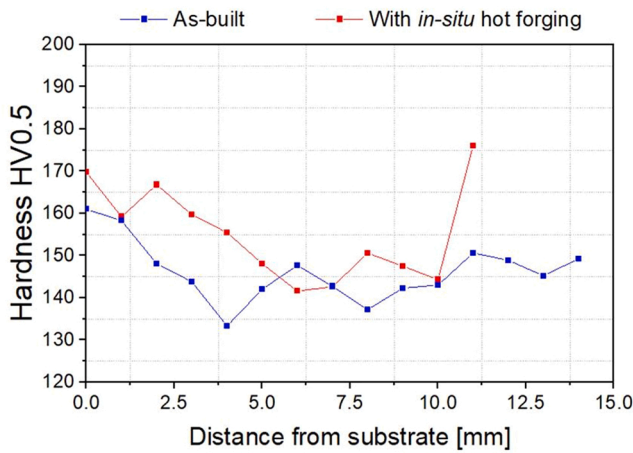


Fig. 8. Hardness measurements across samples height.

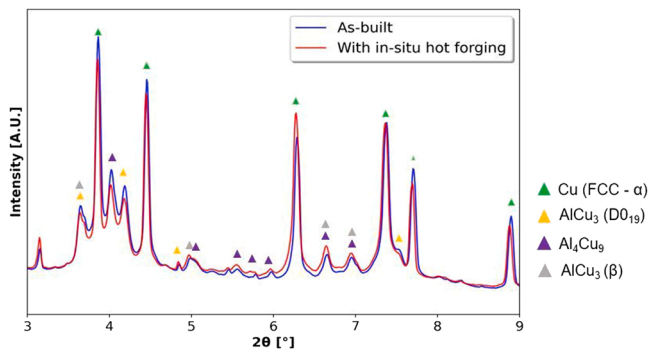


Fig. 9. Diffractogram of samples with and without *in-situ* hot forging.

$$\sigma_{z,k} = \frac{E}{(1+\nu)(1-2\nu)} [(1-\nu)\epsilon_{z,k} + \nu(\epsilon_{xx,k} + \epsilon_{yy,k})] \quad (14)$$

Finally, the equivalent von Mises stress was also calculated for each sample according to Eq. (15).

$$\sigma_{eq} = \sqrt{\frac{1}{2} [(\sigma_x - \sigma_y)^2 + (\sigma_y - \sigma_z)^2 + (\sigma_x - \sigma_z)^2]} \quad (15)$$

5. Results and discussion

Fig. 5 depicts the upper and side surfaces of the produced samples. In the as-built sample the difference in height at the beginning of each layer occurs due to rapid cooling and the small amount of heat accumulated, in contrast to the remaining of the sample where the colling conditions are stable and constant. Usually, to correct this, it is required an in-line parametric correction. It is evident that the hammer has a considerable impact on the sample geometry as it flattens the layers, thereby diminishing this feature that needs correction. In the hot forged sample, the flat top surfaces are achieved due to the constant process conditions of the *in-situ* hot forging.

The temperature at which the material is forged is controlled by the following process conditions: deposition parameters, that define the temperature gradient along the horizontal direction; and the distance from the hammer to the electric arc. Since both conditions are kept constant, the material forging temperature and, therefore, its properties are constant, promoting an evenly distributed flat surface. Moreover, this flattening effect of the deposited layer assists in the deposition of the subsequent layer.

The geometry of the forged sample may change depending on various parameter. If the deposition parameters are set with a higher

heat input, the forging temperature is higher and more deformation will be imposed, increasing the layer width and reducing its height. Additionally, to increase the deformation, the hammer can also be placed closer to the electric arc and the pneumatic pressure can also be increased.

The alloy did not present significant problems under WAAM, with the internal structure being free of porosities and cracks as expected [24]. However, the high thermal conductivity of these alloys tends to produce irregular lateral surfaces, and a part built in height tends to be irregular due to non-confined material flow, as shown in the macrographs of Fig. 6.

5.1. Microstructure

During additive manufacturing of metals, the deposition of a layer causes repeated thermal cycles in the previously deposited layers which can significantly affect their microstructure, promoting different grain sizes along the build direction [25,26]. At the bottom of both samples a finer microstructure was observed, which is caused by the rapid cooling due to the heat dissipated to the cold substrate. The middle layers have the coarser grains of the sample, because the heat flow is lower than in the first layers, and therefore the cooling rate is also lower, in addition to the thermal cycles caused by the following depositions that promote grain growth. Lastly, in the upper layers, the grain size is smaller than in the middle layers, since they are subjected to less thermal cycles than the layers below.

However, looking into the microstructures depicted for both samples in Fig. 7, it is evident that the hot forged AM sample has a finer microstructure and that it is uniform in height, *e.g.*, it is almost independent of the number of layers deposited on top of each other, while the as-built part has a coarser microstructure. Additionally, both samples have a primary β phase (dark regions) in the grain boundaries and α phase (bright regions) inside the grains in a cellular-dendritic morphology. The α phase has an face-centered cubic (FCC) crystal structure while β phase has a body-centered cubic (BCC) structure [27]. The identification of the alpha and beta phases were made according to the existing literature [28,29].

The average columnar dendrites width measured on the as-built sample was of $23.2 \pm 5.2 \mu\text{m}$, while in the hot forged sample was of $11.4 \pm 2.3 \mu\text{m}$, corresponding to a grain size reduction of $\approx 51\%$. Another interesting feature is that the forged sample has a higher β phase fraction, which can be seen in the micrographs (Fig. 7) but also in the diffractograms depicted in Fig. 9. Previous studies on Cu-Al alloys [30], showed that pressure may affect the solid state transformation and consequently the phase fraction, *i.e.* with an increase in pressure there is an increase in β phase volume fraction and vice versa. The *in-situ* hot forging promotes a momentary increase of the material pressure while it is at $750 \text{ }^\circ\text{C}$, which affect the phase transformation and increases the volume fraction of the β phase.

Hardness values are of $145 \pm 6 \text{ HV}$ and $155 \pm 9 \text{ HV}$ for the as-built and the *in-situ* hot forged samples respectively, as shown in Fig. 8. The increase of β phase fraction may explain the slight increase in hardness despite the significant reduction of grain size.

X-ray synchrotron radiation also shows that the *in-situ* hot forging operation has no effect on the identified phases as shown in Fig. 9. However, from the 2D Debye-Scherrer diffractograms it can be observed that the as-built part has a coarser and textured microstructure, while the hot forged one has a homogeneous more isotropic fine-grained microstructure with almost no texture (Fig. 10).

To evaluate the influence of the *in-situ* hot forging on the mechanical properties and anisotropy of the deposited material, uniaxial compression tests were preferred over tensile ones, which allowed to evaluate specific zones in different directions using reduced sized specimens.

The results of the mechanical tests performed are in agreement with the above considerations on the microstructure. Representative compression stress-strain curves for each sample obtained at different

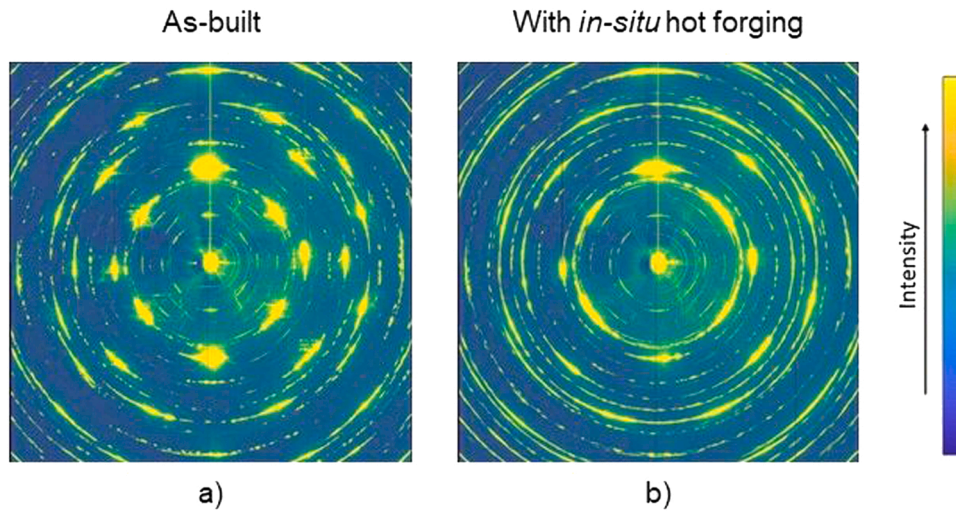


Fig. 10. 2D Debye-Scherrer patterns of samples: as-built (a) and *in-situ* hot forged (b).

orientations are depicted in Fig. 11. The summary of these compression tests is further detailed in Table 3. It can be observed that the use of *in-situ* hot forging during WAAM of the CuAl8 results in more isotropic mechanical properties. In particular, the yield strength of the hot forged samples is identical in the specimens obtained in the vertical and horizontal directions, while those obtained without *in-situ* hot forging presented a higher yield strength in the horizontal direction. The large and highly oriented grains in the CuAl8 deposits made without *in-situ* hot forging justify this variation. The compressive strength of the parts was also seen to show similar values for the vertical and horizontal *in-situ* hot forged CuAl8 WAAM parts, while for the as-built sample a difference of more than 100 MPa was determined. These results further highlight the potential of *in-situ* hot forging WAAM in contributing to a microstructure refinement by breaking the large columnar grain structure typical of WAAM, which then results in more isotropic mechanical properties. Fracture always occurred at approximately 45° with the applied force direction, as expected for a ductile alloy as this one.

Since CuAl8 alloys are used in electromagnetic applications, the electrical conductivity was measured to assess, whether the effect of the *in-situ* hot forging reduced this property. Fig. 12 depicts the electrical conductivity profiles along the height of the parts, and there is a negligible difference, showing that the *in-situ* hot forging WAAM does not significantly affect the electric conductivity of this alloy, which can be

Table 3

Summary of mechanical properties.

| Direction of sample removal | | Yield strength [MPa] | Compressive strength [MPa] |
|-----------------------------|---------------------|----------------------|----------------------------|
| Vertical | With hot forging | 258 ± 33 | 1362 ± 64 |
| | Without hot forging | 245 ± 15 | 1334 ± 79 |
| Horizontal | With hot forging | 246 ± 13 | 1349 ± 42 |
| | Without hot forging | 292 ± 26 | 1216 ± 20 |

beneficial.

The fact that this alloy has an excellent electrical conductivity, prevents to have an identification of the grain refined zones in the manufactured parts, as observed in other alloys. Nevertheless, this method is sensitive to microstructural features as discussed by Santos et al. [19], and it is evident that the as-built part has a coarser microstructure due to more pronounced peaks and valleys.

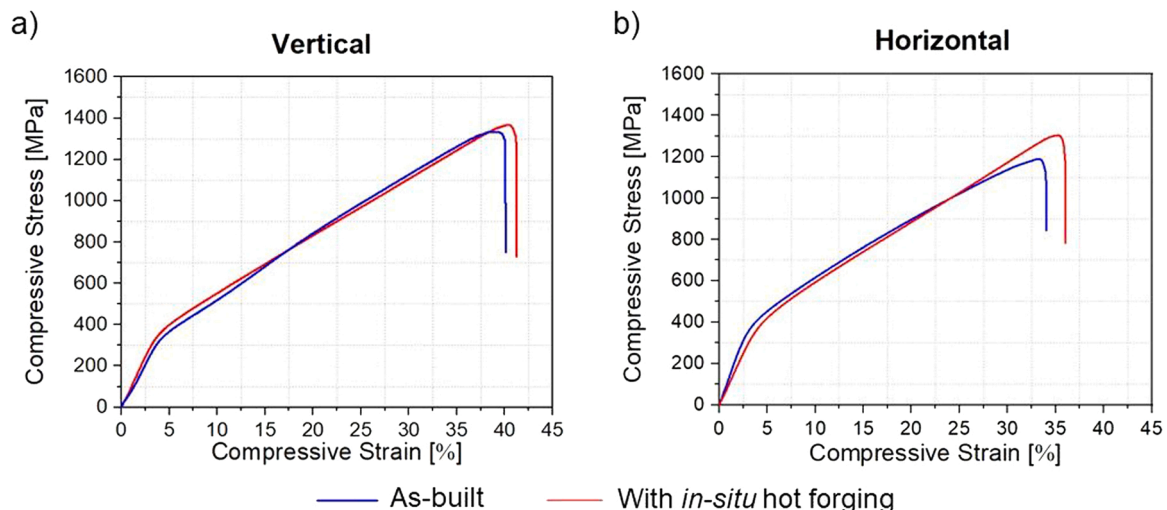


Fig. 11. Uniaxial compression stress-strain curves for the samples removed from horizontal a) and vertical b) directions of the as-built and *in-situ* hot forged samples.

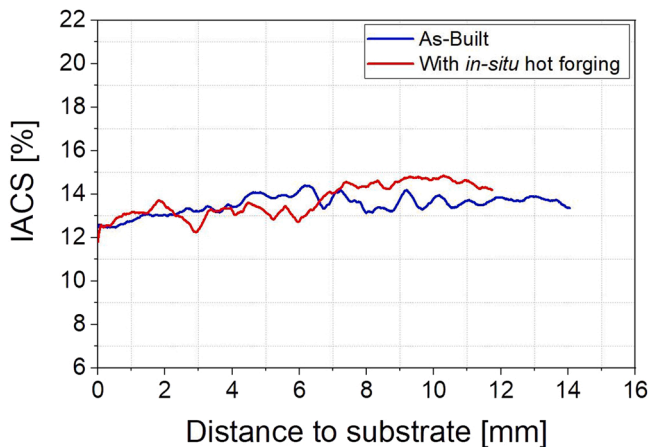


Fig. 12. Comparison of the electrical conductivity along the height of the parts with and without *in-situ* hot forging. IACS means “International Annealed Copper Standard”, and it expresses the electric conductivity as a percentage of the conductivity of pure annealed copper at 20° C. 100% IACS corresponds to an electric conductivity of 58×10^6 S/m.

5.2. Residual stress measurements

In conventional WAAM parts, distortion builds up due to the accumulation of residual stresses that are formed as a consequence of the thermal gradients during the deposition process, with the same formation mechanism as those discussed in the arc welding process [31]. To satisfy the equilibrium condition, the residual stresses present on a part must always be balanced in such a way that the resultant force is null. Moreover, the magnitude and direction of these stresses depend, among others, on the material, the deposition strategy and parameter selection, as well as the dimensions and geometry of the component.

In WAAM, research most studies are performed on thin-walled samples, and the analysis of residual stress is focused on three directions: longitudinal (X axis); transverse (Z axis) and normal (Y axis), as illustrated in Fig. 13. Among these, the directions where the development of residual stresses due to the thermal gradients is more critical are the longitudinal and normal directions, since along the transverse direction, the low width of the wall samples restricts the development of large residual stresses.

Additionally, regarding the longitudinal stresses measured along the building direction, after unclamping the part from the baseplate, the specimen typically bent upwards to balance the net bending moment across the section and achieve the equilibrium condition, and tensile stress are observed at the bottom of the wall and steadily decreased towards the top, where they tend show a compressive nature. Moreover, the geometry of the substrate also influences the stress development on the deposited material. For depositions with few layers where the substrates accounts for a large amount of the total part height, the neutral axis can be positioned over the substrate, which puts all the deposited material under compressive residual stresses, as observed by Moat et al.

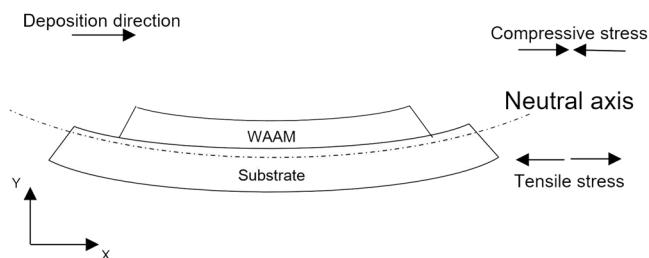


Fig. 13. Schematic representation of the longitudinal stress distribution in a WAAM part after unclamping.

[32] and is illustrated in Fig. 13. While for higher samples where the substrate is a small percentage of the total part height, the neutral axis is positioned over the deposited material, and therefore, near the substrate the deposited material is under tensile residual stress and in the upper region it is under compressive stresses [33–35].

The directional and equivalent residual stress measurements as obtained from the high energy synchrotron X-ray diffraction measurements are shown in Fig. 14. As expected, the transverse residual stress along the sample height is almost null in both samples. It is also observed that most of the longitudinal and normal tensile stresses are accommodated by the substrate, indicating that the neutral axis is situated near the interface between the substrate and the deposited material.

In the as-built sample, the stresses aligned with the longitudinal direction present a profile in agreement with the ones reported in the bibliography [35], where it is verified that from the bottom of the wall towards the top the stress steadily decreased.

It is clear that the *in-situ* hot forging reduces the magnitude of the residual stress formed due to thermal gradients in both longitudinal and normal directions. But the most relevant is the fact that the longitudinal stresses, instead of presenting a curvature with a negative slope, present an almost constant stress value along the height of the sample, which indicates that the material will have the same behavior regardless of the location where an external load may be applied. Moreover, the compressive residual stresses may also positively affect fatigue crack growth in both normal and longitudinal directions.

The variation in the magnitude of residual stresses due to forging occurs during the production of the part while the substrate is still clamped. When the material cools down to room temperature, after its deposition, the material wants to shrink due to the thermal contraction, but since the substrate is clamped, it limits this contraction of the material and therefore tensile stresses are developed. The *in-situ* hot forging occurs immediately after the deposition of the material, and the compressive stresses induced by the forging counteract the tensile stresses induced by thermal gradients. Thus, after unclamping the part, the stress redistribution needed to reach an equilibrium state is lower in the hot forged sample than in the as-built one, since the resultant magnitude of the residual tensile stresses is lower due to the positive effect induced by the compressive stress introduced by the hot forging.

Moreover, from a distance of 10 mm from substrate, a rapidly increase of the von Mises equivalent stress is observed in the *in-situ* hot forged sample, which is where the last layer starts, and thus the total compressive residual stresses formed during forging are still present since there is no subsequent layer to partially remelt the forged material. This is corroborated by the measurements of the principal stresses showed in Fig. 14a), where an increase of the compressive stresses is observed in the hot forged sample, particularly in the normal (Y axis) and longitudinal (X axis) directions, in contrast to the as-built sample.

6. Conclusions

This paper presents the results of a study performed in *in-situ* hot forging wire and arc additive manufacturing of a CuAl8 alloy with a circular hammer to improve the forged area, while allowing to produce part shapes other than linear. A dynamic study of the process is presented analyzing the forces applied in the visco-plastic regime. The following major conclusions were drawn:

- The CuAl8 alloy does not develop defects during arc-based additive manufacturing with or without the *in-situ* hot forging variant;
- the application of *in-situ* hot forging clearly refines and homogenizes the microstructure without significantly affecting the existing phases. Qualitatively, the hot forging operation seems to slightly increase the β phase fraction;
- since this is a highly ductile alloy there is no significant variation in hardness;

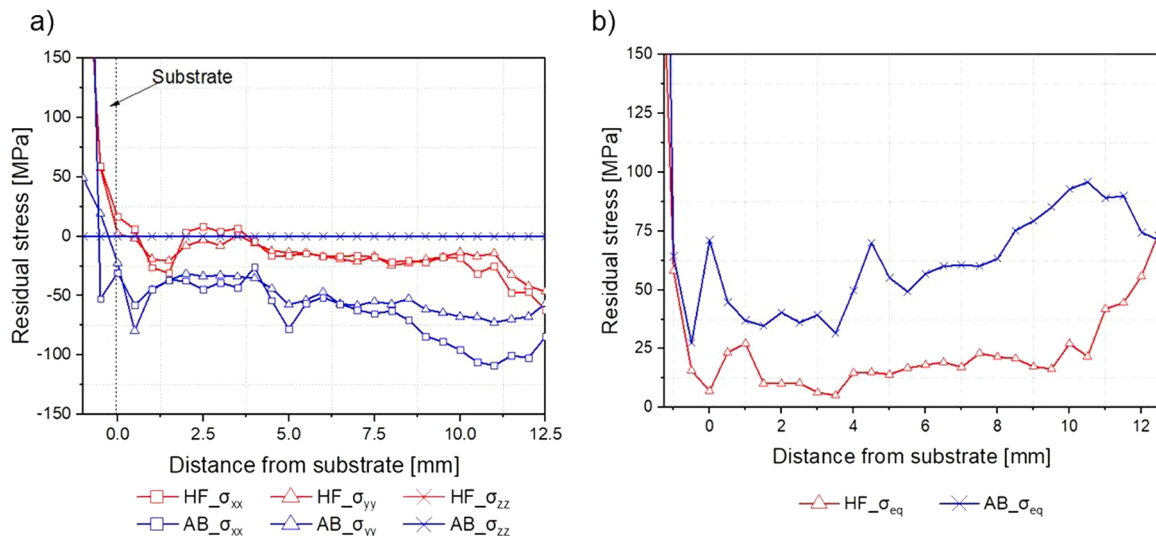


Fig. 14. Residual stresses measured by synchrotron X-ray diffraction in the as-built and *in-situ* hot forged samples: a) principal stresses; b) von Mises equivalent stress. The “HF” red curve corresponds to the *in-situ* hot forged condition while “AB” blue curve corresponds to the as-build condition.

- compressive strength measured showed a more homogeneous resistance in vertical and horizontal directions when the part is hot forged, while the as-built part has a more significant difference in both directions. As expected, fracture occurred at approximately 45°;
- hot forging does not affect the electrical conductivity of WAAM parts;
- hot forging reduces and homogenize the residual stress of parts.

CRediT authorship contribution statement

Telmo G. Santos: Writing – review & editing, Supervision, Project administration, Funding acquisition, Conceptualization. **João P. Oliveira:** Writing – review & editing, Supervision, Data curation, Conceptualization. **Rosa M. Miranda:** Writing – review & editing, Writing – original draft, Supervision, Conceptualization. **Norbert Schell:** Resources, Investigation. **Tiago A. Rodrigues:** Software, Investigation, Data curation. **Valdemar R. Duarte:** Writing – original draft, Investigation, Conceptualization.

Declaration of Competing Interest

The authors declare that they have no known competing financial interests or personal relationships that could have appeared to influence the work reported in this paper.

Acknowledgments

Authors acknowledge the Portuguese Fundação para a Ciência e a Tecnologia (FCT - MCTES) for its financial support *via* the project UID/EMS/00667/2019 (UNIDEMI). VD acknowledges Portuguese Fundação para a Ciência e a Tecnologia (FCT - MCTES) for funding the PhD grant SFRH/BD/139454/2018. TAR acknowledges Portuguese Fundação para a Ciência e a Tecnologia (FCT - MCTES) for funding the PhD grant SFRH/BD/144202/2019. Funding of CENIMAT/i3N by national funds through the Portuguese Fundação para a Ciência e a Tecnologia, I.P., within the scope of Multiannual Financing of R&D Units, reference UIDB/50025/2020–2023 is also acknowledge. This activity has received funding from the European Institute of Innovation and Technology (EIT) Raw Materials through the project Smart WAAM: Microstructural Engineering and Integrated Non-Destructive Testing. This body of the European Union receives support from the European Union’s Horizon 2020 research and innovation programme. Parts of this research were carried out at PETRA III at DESY, a member of the Helmholtz Association. The research

leading to this result has been supported by the project CALIPSOplus under the Grant Agreement 730872 from the EU Framework Programme for Research and Innovation HORIZON 2020. This project has received funding from the EU-H2020 research and innovation programme under grant agreement No 654360 having benefitted from the access provided by PETRA III at DESY in Hamburg, Germany within the framework of the NFFA-Europe Transnational Access Activity. The authors acknowledge support by OCAS NV and GUARENTEED *via* Joachim Antonissen.

Remark: The supplementary material is temporarily available in the Drive folder here: <https://drive.google.com/drive/folders/1SFFlhJmL5p3IkQis8cB6UVVva3wozGi?usp=sharing>.

Appendix A. Supporting information

Supplementary data associated with this article can be found in the online version at [doi:10.1016/j.addma.2022.102847](https://doi.org/10.1016/j.addma.2022.102847).

References

- [1] T. DebRoy, H.L. Wei, J.S. Zuback, T. Mukherjee, J.W. Elmer, J.O. Milewski, A. M. Beese, A. Wilson-Heid, A. De, W. Zhang, Additive manufacturing of metallic components – process, structure and properties, *Prog. Mater. Sci.* 92 (2018) 112–224, <https://doi.org/10.1016/j.pmatsci.2017.10.001>.
- [2] T.A. Rodrigues, V. Duarte, R.M. Miranda, T.G. Santos, J.P. Oliveira, Current status and perspectives on wire and arc additive manufacturing (WAAM), *Materials* 12 (2019) 1121, <https://doi.org/10.3390/ma12071121>.
- [3] J.P. Oliveira, T.G. Santos, R.M. Miranda, Revisiting fundamental welding concepts to improve additive manufacturing: from theory to practice, *Prog. Mater. Sci.* (2019), 100590, <https://doi.org/10.1016/j.PMATSCI.2019.100590>.
- [4] ASM International, *Weld Solidification*, in: *Weld Integr. Perform.*, 1997: p. 19.
- [5] A.R. McAndrew, M. Alvarez Rosales, P.A. Colegrove, J.R. Hönnige, A. Ho, R. Fayolle, K. Eytayo, I. Stan, P. Sukrongpan, A. Crochemore, Z. Pinter, Interpass rolling of Ti-6Al-4V wire + arc additively manufactured features for microstructural refinement, *Addit. Manuf.* 21 (2018) 340–349, <https://doi.org/10.1016/J.ADDMA.2018.03.006>.
- [6] M.A. Easton, M. Qian, A. Prasad, D.H. StJohn, Recent advances in grain refinement of light metals and alloys, *Curr. Opin. Solid State Mater. Sci.* 20 (2016) 13–24, <https://doi.org/10.1016/J.COSSMS.2015.10.001>.
- [7] L.J. da Silva, D.M. Souza, D.B. de Araújo, R.P. Reis, A. Scotti, Concept and validation of an active cooling technique to mitigate heat accumulation in WAAM, *Int. J. Adv. Manuf. Technol.* 107 (2020) 2513–2523, <https://doi.org/10.1007/s00170-020-05201-4>.
- [8] D. Ding, B. Wu, Z. Pan, Z. Qiu, H. Li, Wire arc additive manufacturing of Ti6Al4V using active interpass cooling, *Mater. Manuf. Process.* 35 (2020) 845–851, <https://doi.org/10.1080/10426914.2020.1732414>.
- [9] H. Zhang, X. Wang, G. Wang, Y. Zhang, Hybrid direct manufacturing method of metallic parts using deposition and micro continuous rolling, *Rapid Prototyp. J.* 19 (2013) 387–394, <https://doi.org/10.1108/RPJ-01-2012-0006/FULL/XML>.
- [10] C. Li, Y. Tian, Y. Chen, P. Hodgson, X. Wu, Y. Zhu, A. Huang, Hierarchical layered and refined grain structure of Inconel 718 superalloy produced by rolling-assisted

- directed energy deposition, *Addit. Manuf. Lett.* 1 (2021), 100009, <https://doi.org/10.1016/J.ADDLET.2021.100009>.
- [11] X. Tian, Y. Zhu, C.V.S. Lim, J. Williams, R. Boyer, X. Wu, K. Zhang, A. Huang, Isotropic and improved tensile properties of Ti-6Al-4V achieved by in-situ rolling in direct energy deposition, *Addit. Manuf.* 46 (2021), 102151, <https://doi.org/10.1016/J.ADDMA.2021.102151>.
- [12] X. Fang, L. Zhang, G. Chen, K. Huang, F. Xue, L. Wang, J. Zhao, B. Lu, Microstructure evolution of wire-arc additively manufactured 2319 aluminum alloy with interlayer hammering, *Mater. Sci. Eng. A* 800 (2021), 140168, <https://doi.org/10.1016/J.MSEA.2020.140168>.
- [13] V.R. Duarte, T.A. Rodrigues, N. Schell, R.M. Miranda, J.P. Oliveira, T.G. Santos, Hot forging wire and arc additive manufacturing (HF-WAAM), *Addit. Manuf.* 35 (2020), 101193, <https://doi.org/10.1016/j.addma.2020.101193>.
- [14] H. Ye, K. Ye, B. Gao Guo, F. Bing Le, C. Wei, X. Sun, G. Yong Wang, Y. Liu, Effects of combining ultrasonic micro-forging treatment with laser metal wire deposition on microstructural and mechanical properties in Ti-6Al-4V alloy, *Mater. Charact.* 162 (2020), 110187, <https://doi.org/10.1016/J.MATCHAR.2020.110187>.
- [15] Q. Li, Y. Zhang, J. Chen, B. Guo, W. Wang, Y. Jing, Y. Liu, Effect of ultrasonic micro-forging treatment on microstructure and mechanical properties of GH3039 superalloy processed by directed energy deposition, *J. Mater. Sci. Technol.* 70 (2021) 185–196, <https://doi.org/10.1016/J.JMST.2020.09.001>.
- [16] V.R. Duarte, T.A. Rodrigues, M.A. MacHado, J.P.M. Pragana, P. Pombinha, L. Coutinho, C.M.A. Silva, R.M. Miranda, C. Goodwin, D.E. Huber, J.P. Oliveira, T.G. Santos, Benchmarking of Nondestructive Testing for Additive Manufacturing, <https://Home.Liebertpub.Com/3dp>. 8 (2021) 263–270. <https://doi.org/10.1089/3DP.2020.0204>.
- [17] T.J. Gomes Santos, V. Rebelo Duarte, T.M. André Rodrigues, J.P. Sousa Oliveira, R. M. Mendes Miranda, System for hot forging wire and arc additive manufacturing, PCT/IB2020/056100, 2020. (<https://patentscope.wipo.int/search/en/detail.jsf?docid=WO2020261233&cid=P11-KWOLW4-04372-1>) (accessed January 17, 2022).
- [18] U. Reisgen, M. Angerhausen, A. Pipinikas, T. Twiehaus, V. Wesling, J. Barthelmie, The effect of arc brazing process parameters on the microstructure and mechanical properties of high-strength steel HCT780XD using the copper-based filler metal CuAl8, *J. Mater. Process. Technol.* 249 (2017) 549–558, <https://doi.org/10.1016/J.JMATPROTEC.2017.06.040>.
- [19] T.G. Santos, P. Vilaça, R.M. Miranda, Electrical conductivity field analysis for evaluation of FSW joints in AA6013 and AA7075 alloys, *J. Mater. Process. Technol.* 211 (2011) 174–180, <https://doi.org/10.1016/j.jmatprotec.2010.08.030>.
- [20] P. Crowther, C.S. Daniel, xrdfit: A Python package for fitting synchrotron X-ray diffraction spectra, *J. Open Source Softw.* 5 (2020) 2381, <https://doi.org/10.21105/JOSS.02381>.
- [21] P.J. Withers, M. Preuss, A. Steuwer, J.W.L. Pang, Methods for obtaining the strain-free lattice parameter when using diffraction to determine residual stress, *J. Appl. Crystallogr.* 40 (2007) 891–904, <https://doi.org/10.1107/S0021889807030269/HTTPS://JOURNALS.IUCR.ORG/SERVICES/TERMSOFUSE.HTML>.
- [22] Copper, UNS C62300 (Aluminum Bronze 9%), (n.d.). (<http://www.matweb.com/search/DataSheet.aspx?MatGUID=f1849aef47fd4057ad25e21899e93ed1&ckck=1>) (accessed January 16, 2022).
- [23] Z. Wang, E. Denlinger, P. Michaleris, A.D. Stoica, D. Ma, A.M. Beese, Residual stress mapping in Inconel 625 fabricated through additive manufacturing: Method for neutron diffraction measurements to validate thermomechanical model predictions, *Mater. Des.* 113 (2017) 169–177, <https://doi.org/10.1016/J.MATDES.2016.10.003>.
- [24] AWS, *Welding handbook, Metals and Their Weldability*, AWS., 1976.
- [25] H. Wang, Z.G. Zhu, H. Chen, A.G. Wang, J.Q. Liu, H.W. Liu, R.K. Zheng, S.M.L. Nai, S. Primig, S.S. Babu, S.P. Ringer, X.Z. Liao, Effect of cyclic rapid thermal loadings on the microstructural evolution of a CrMnFeCoNi high-entropy alloy manufactured by selective laser melting, *Acta Mater.* 196 (2020) 609–625, <https://doi.org/10.1016/J.ACTAMAT.2020.07.006>.
- [26] Y. Lu, S. Su, S. Zhang, Y. Huang, Z. Qin, X. Lu, W. Chen, Controllable additive manufacturing of gradient bulk metallic glass composite with high strength and tensile ductility, *Acta Mater.* 206 (2021), 116632, <https://doi.org/10.1016/J.ACTAMAT.2021.116632>.
- [27] O. Zobac, A. Kroupa, A. Zemanova, K.W. Richter, Experimental description of the Al-Cu binary phase diagram, *Metall. Mater. Trans. A Phys. Metall. Mater. Sci.* 50 (2019) 3805–3815, <https://doi.org/10.1007/S11661-019-05286-X/FIGURES/8>.
- [28] S.E. Mousavi, A. Sonboli, N. Naghshehkish, M. Meratian, A. Salehi, M. Sanayei, Different behavior of alpha and beta phases in a Low Stacking Fault Energy copper alloy under severe plastic deformation, *Mater. Sci. Eng. A* 788 (2020), 139550, <https://doi.org/10.1016/J.MSEA.2020.139550>.
- [29] T.A. Rodrigues, N. Bairrão, F.W.C. Farias, A. Shamsolhodaei, J. Shen, N. Zhou, E. Maawad, N. Schell, T.G. Santos, J.P. Oliveira, Steel-copper functionally graded material produced by twin-wire and arc additive manufacturing (T-WAAM), *Mater. Des.* 213 (2022), 110270, <https://doi.org/10.1016/J.MATDES.2021.110270>.
- [30] L. Gong, L. Jian-Hua, W. Wen-Kui, L. Ri-Ping, Influence of pressure on the solid state phase transformation of Cu–Al–Bi alloy, *Chin. Phys. B* 19 (2010), 096202, <https://doi.org/10.1088/1674-1056/19/9/096202>.
- [31] H.E. Coules, P. Colegrove, L.D. Cozzolino, S.W. Wen, Experimental measurement of biaxial thermal stress fields caused by arc welding, *J. Mater. Process. Technol.* 212 (2012) 962–968, <https://doi.org/10.1016/j.jmatprotec.2011.12.006>.
- [32] R.J. Moat, A.J. Pinkerton, L. Li, P.J. Withers, M. Preuss, Residual stresses in laser direct metal deposited Waspaloy, *Mater. Sci. Eng. A* 528 (2011) 2288–2298, <https://doi.org/10.1016/J.MSEA.2010.12.010>.
- [33] P.A. Colegrove, H.E. Coules, J. Fairman, F. Martina, T. Kashoob, H. Mamash, L. D. Cozzolino, Microstructure and residual stress improvement in wire and arc additively manufactured parts through high-pressure rolling, *J. Mater. Process. Technol.* 213 (2013) 1782–1791, <https://doi.org/10.1016/j.jmatprotec.2013.04.012>.
- [34] B.A. Szost, S. Terzi, F. Martina, D. Boisselier, A. Prytuliak, T. Pirling, M. Hofmann, D.J. Jarvis, A comparative study of additive manufacturing techniques: Residual stress and microstructural analysis of CLAD and WAAM printed Ti-6Al-4V components, *Mater. Des.* 89 (2016) 559–567, <https://doi.org/10.1016/j.matdes.2015.09.115>.
- [35] F. Martina, M.J. Roy, B.A. Szost, S. Terzi, P.A. Colegrove, S.W. Williams, P. J. Withers, J. Meyer, M. Hofmann, Residual stress of as-deposited and rolled wire+arc additive manufacturing Ti-6Al-4V components, *Mater. Sci. Technol.* 32 (2016) 1439–1448, <https://doi.org/10.1080/02670836.2016.1142704>.